Stress Heterogeneities in Earthquake Rupture Experiments with Material Contrasts

Sebastian Langer[a,*], Dion Weatherley[b], Louise Olsen-Kettle[a], Yaron Finzi[a]

[a] *Earth Systems Science Computational Centre, School of Earth Sciences, The University of Queensland, Brisbane, Australia.*

[b] *WH Bryan Mining and Geology Research Centre, Sustainable Minerals Institute, The University of Queensland, Brisbane, Australia.*

Abstract

We investigate significant heterogeneous stresses along bimaterial interfaces in laboratory and numerical experiments. These stresses, partially induced by model or experimental configuration, affect the supershear transition length and rupture speed, mode and directivity in uniaxial compression tests and dynamic rupture experiments with bimaterial interfaces. Using numerical simulations we show that normal and tangential stresses at the fault are distorted by the different stress-strain relationships of the materials. This distortion leads to altered supershear transition lengths, higher rupture potencies and amplifies the preference for rupture in the direction of slip of the slower and more compliant material. We demonstrate how this stress-distortion can be decreased in laboratory experiments by using larger specimen samples and in numerical models by using periodic boundary conditions.

Keywords: bimaterial interface, dynamic rupture, stress heterogeneities, supershear transition, laboratory experiment, elastic moduli, rupture directivity, numerical fault model

1. Introduction

Rupture propagation directly affects the growth and eventual size of earthquakes, the energy radiation patterns and the resulting ground motions that induce tsunamis, landslides and damage to infrastructure. As large earthquakes often occur along faults separating dissimilar materials, dynamic rupture along bimaterial interfaces is extensively studied to improve seismic hazard analysis. Theoretical studies investigate the fundamental physical processes as a starting point to understand rupture propagation along such interfaces (Rayleigh, 1885; Weertman, 1963). However, comparing analytical results with laboratory experiments and numerical models is difficult due to significant effects of apparatus design (loading and confinement methods), numerical procedures and boundary conditions. Due to stress heterogeneities introduced in experiments and

*Corresponding author. Tel.: +61 7 334 64096. Fax.: +61 7 334 64134
Email address: s.langer@uq.edu.au (Sebastian Langer)
URL: http://esscc.uq.edu.au (Sebastian Langer)

models, complex behavior may emerge in even the simplest setups, resulting in rupture characteristics different from those derived theoretically (Anderson, 1972). To better understand the natural phenomena in this work we try to resolve the differences between various experiments and models and evaluate how well they represent in-situ processes.

Ruptures propagating along bimaterial faults generate large dynamic changes of the normal stress along the fault. These stress perturbations influence rupture velocities and potencies differently along the positive rupture direction (direction of slip of the more compliant material) and the negative rupture direction (direction of slip of the stiffer material) (Weertman, 1980; Andrews and Ben-Zion, 1997). This so called "bimaterial effect" occurs for sub-Rayleigh ruptures and is a result of normal stress change *behind* the rupture tip. Subshear ruptures have higher rupture velocities in the positive direction due to a tensile stress perturbation *behind* the rupture tip which follows the rupture front and promotes rupture (Weertman, 1980; Andrews and Ben-Zion, 1997; Rubin and Ampuero, 2007). Subshear ruptures therefore exhibit higher potencies in the positive direction and a preference for this direction in bilateral ruptures (Ben-Zion, 2001; Ampuero and Ben-Zion, 2008; Langer et al., 2010). Conversely, in the negative direction the sign of the normal stress change is reversed (compressive) *behind* the rupture tip leading to dynamic strengthening and lower rupture velocities for subshear rupture.

The possibility of rupture travelling at speeds faster than the Rayleigh wave speed (Rayleigh, 1885) has been shown analytically by Burridge (1973). Andrews (1976) showed numerically that a rupture can transition from sub-Rayleigh to supershear speeds by the occurrence of a daughter crack in front of the crack-tip which then unites with the mother crack and travels at the primary wave speed. Experiments by Xia et al. (2004) showed the existence of this so-called Burridge-Andrews mechanism for transition into supershear. Supershear rupture propagation has also been observed in nature during the 2001 Kunlunshan (Bouchon and Vallée, 2003), the 2002 Denali (Dunham and Archuleta, 2004) and the 2010 Qinghai earthquakes (Wang and Mori, 2012). All three earthquakes started at propagation speeds below the shear wave velocity and then transitioned to supershear speeds. An interesting result of both numerical and analytical studies, is that supershear rupture along bimaterial interfaces occurs predominantly (Harris and Day, 1997; Shi and Ben-Zion, 2006; Langer et al., 2012) or exclusively (Ranjith and Rice, 2001; Adams, 2001; Cochard and Rice, 2000) in the negative direction. Our recent numerical simulations showed that the normal stress changes in *front* of the rupture tip influence whether or not a supershear transition will occur (Langer et al., 2012). The supershear transition is enhanced in the negative direction, where normal stress changes ahead of the rupture unclamp the fault, making it easier for the shear wave stress peak to trigger supershear failure of the fault. The opposite applies in the positive direction, such that the transition is delayed or sometimes even suppressed.

In the current work we show that the directivity and supershear transition are influenced by

the stress-distortions along the interface and we quantify the extent of these distortions for various experimental and numerical model setups. We also show that increasing the specimen size in laboratory experiments may reduce the stress-distortions and that they can be removed completely by using periodic boundaries in numerical simulations. We add to the growing literature that has studied the influence of finite-size and edge effects and their subsequent stress-distortions which need to be taken into consideration for the interpretation of experimental and numerical results.

Many experimental studies have investigated the above mentioned earthquake rupture characteristics. An important feature of such laboratory model setups is the finite specimen size that introduces edge effects and influences the outcome of rupture experiments. This shortcoming was addressed in work by Scholz et al. (1972), where in a direct shear test a rock slab was forced to slide between two stationary slabs, producing a large moment, that resulted in a high stress gradient over the sliding surfaces. Thus Scholz et al. (1972) stated, that "... frictional results from direct shear experiments cannot be related directly to parameters of interest such as the shear or normal stresses." Lambros and Rosakis (1994) and Rosakis et al. (1998) avoided these loading-induced stress-distortions, as they did not load their specimens prior to rupture nucleation. They subjected an uncompressed specimen to one-point impact-loading near the fault at one boundary of the specimen. Subsequent work decoupled the loading and the initiation of slip along the fault. Xia et al. (2004) and Xia et al. (2005) subjected their specimens to uniaxial compression, mimicking slow tectonic loading, where the angle between their fault face and the applied far-field loading did not allow the fault to slip. They then nucleated dynamic rupture by an exploding wire mechanism, implemented in the center of the fault. As in the experiments with impact-loading they were able to prepare a controlled environment with desired conditions for rupture and then decide on the initiation of rupture rather than having to rely on self-nucleation as in Scholz et al. (1972). These experiments were used to document and characterize supershear transition along material interfaces (Xia et al., 2005). In more recent experiments, Ben-David et al. (2010) and Ben-David and Fineberg (2011) studied frictional sliding by pressing together two PMMA blocks (polymethyl-methacrylate blocks) and applying external shear forces to the top and/or bottom block. They observed highly non-uniform normal and shear stresses caused not only by edge effects, but also by the roughness and geometry of the contact area when loading a homogeneous material interface. They also suggest, that local static friction significantly depends on loading details. From these previous experiments it can be seen, that finite-size effects and stress-distortions may lead to inaccurate interpretation of experimental and numerical results.

In section 2 we outline the numerical method we use to simulate dynamic rupture along bimaterial interfaces and introduce three commonly used experimental or numerical model configurations used for comparison in this work. Section 3 quantifies the magnitude of stress-distortions due to experimental or model setup present in the three different configurations. This section also shows

how to achieve distortion free elastic deformation when periodic boundary conditions are applied in numerical models. It also investigates the influence of stress-distortions due to model setup on sub- and supershear rupture along bimaterial interfaces. In section 4 we summarize the effects of stress heterogeneities due to model setup on rupture characteristics and the implications for interpretation of laboratory experiments and numerical simulations.

2. Comparison of numerical models of dynamic rupture along bimaterial interfaces

2.1. Different setups for simulation of laboratory and in-situ processes

Uniaxial compression tests consisting of quasi-static loading and subsequent dynamic rupture are simulated using the Finite Element Method implemented in the ESYS.ESCRIPT software (Gross et al., 2007; Langer et al., 2010). Triangular meshes are constructed using Gmsh (Geuzaine and Remacle, 2009) with variable mesh size ranging from 1 mm at the outer boundary to 500 μm along the fault. The models include an absorbing boundary layer and in some simulations we adapt the mesh in order to use periodic boundary conditions.

In our simulations we use three different forms of loading conditions to closely model laboratory setups and numerical methods. These are shown in Figure 1. The first model configuration is called the confined configuration. As Figure 1a shows the model is fully confined along the Northern and Southern boundaries. This type of confinement is used by Xia et al. (2005). When the pressure P is applied to the model, there is no normal or tangential movement of the specimen relative to the platens of the hydraulic press. The top and the bottom of the specimen retain their initial size.

As the platens are much stiffer and have a Poisson's ratio $\nu \approx 0$ (and $\nu = 0$ in our numerical model) a shear moment between the platens and the specimen is introduced. This causes buckling of the specimen at its Eastern and Western boundaries as shown in Figure 1a. The second model configuration is called the horizontally unconfined configuration. In contrast to the confined configuration tangential movement at the contact surface between the hydraulic press and the specimen is allowed. Unconfined lateral movement has been used in fracture mechanics numerical models (Tang et al., 2000) and mimics a 'friction reducer' as applied in laboratory compression tests (Labuz et al., 1996). By using such a configuration we remove the distorting influence of the two 'welded' connections between platens and specimen, as these introduce two additional bimaterial interfaces to the model. The third model is often used in numerical simulations and does not involve confinement at the model boundaries. It is called the fully unconfined configuration where far-field loading is applied at the model boundaries as in Harris and Day (1997); Andrews and Ben-Zion (1997) or Shi and Ben-Zion (2006). In most numerical models where a fault separates two dissimilar materials, the fault is aligned with one of the model boundaries as in Figure 1c. The pressure applied is oriented at the same angle β to the fault as in Figures 1a and 1b.

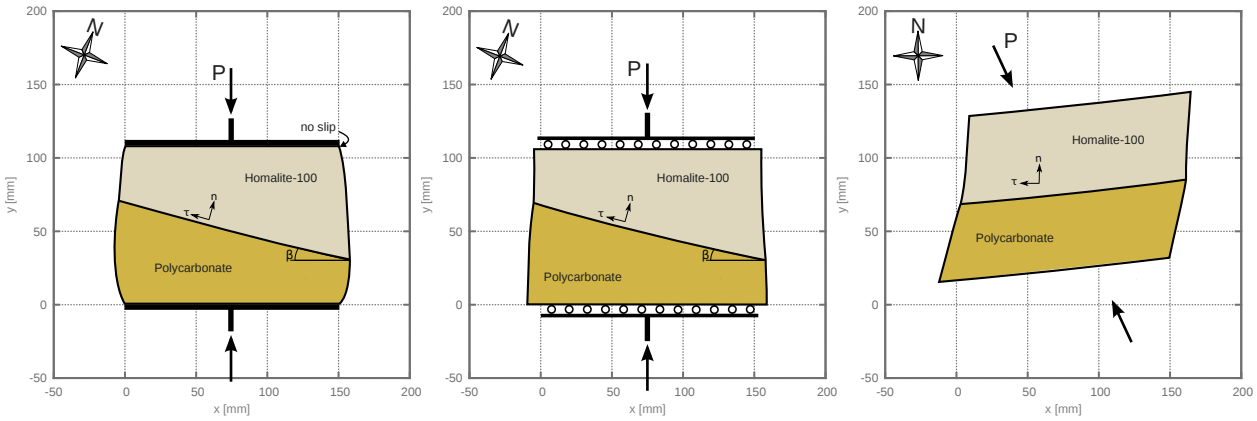

(a) confined configuration (b) horizontally unconfined configuration (c) fully unconfined configuration

Figure 1: (a) shows the confined configuration where neither normal nor tangential displacement between the hydraulic press and the specimen is allowed. (b) shows the horizontally unconfined configuration where only tangential displacement between the hydraulic press and the specimen is allowed. (c) shows the fully unconfined configuration where a far-field stress field is applied with no confinement at the boundaries. All figures show the displacement for $P = -10\,\mathrm{MPa}$ with a 100-fold exaggeration.

For all our simulations we use two materials Homalite-100 and Polycarbonate with the material properties as in Table 1. Homalite-100 is a thermoset polyester, commonly used in dynamic fracture studies (Ravi-Chandar and Knauss, 1984; Ravi-Chandar, 2004, p. 204) and in studies of rupture propagation along a damaged material interface (Bhat et al., 2010; Biegel et al., 2010); Homalite-100 is the stiffer material slipping eastwards (to the right) in our simulations. Polycarbonate is a thermoplastic polymer, capable of significant inelastic deformation (Ravi-Chandar, 2004, p. 207). The three models all have the same size of 150 mm x 150 mm. This means, that each of the models contains the same amount of material. Also due to the fault running through the center of the models there is always an equal amount of Homalite-100 and Polycarbonate involved.

2.2. Quasi-static loading

The horizontally unconfined configuration and the confined configuration are loaded by prescribing a vertical displacement to the top boundary of the specimen. In a first deformation step, the displacement of the top boundary is found by taking the average Young's modulus of the model domain and calculating the vertical displacement under compression with the pressure P. We obtain a solution for the elastic deformation equation $\sigma_{ij,j} = 0$ as in Langer et al. (2010). We determine the component σ_{22} of the stress tensor in the model domain, which is aligned with the direction of P. In the second and last step, the displacement necessary to result in $\sigma_{22} = P$ is calculated and the top boundary is displaced. For the fully unconfined configuration an ambient

Table 1: Material properties, derived from P- and S-wave speeds and densities as given by Xia et al. (2005).

Description	Parameter	Homalite-100	Polycarbonate
Rigidity modulus	μ [GPa]	1.8	1.1
Lamé's first parameter	λ [GPa]	4.2	3.5
Poisson's ratio	ν	0.35	0.38
Density	ρ [g/cm^3]	1.262	1.192
Rayleigh wave velocity	C_R [m/s]	1122	902
Shear wave velocity	C_S [m/s]	1200	960
Primary wave velocity	C_P [m/s]	2498	2182

stress field is applied over the model domain. The pressure P is rotated into the stress tensor σ to obtain the same orientation as for the confined and horizontally unconfined configurations. The stress tensor is applied and the displacement of the mesh elements is calculated in a single step. We are then able to obtain the normal force σ_N and tangential force τ along the bimaterial interface as well as the parameter S (Andrews, 1976), calculated as

$$S = \frac{\mu_s \left|\sigma_N\right| - \left|\tau\right|}{\left|\tau\right| - \mu_d \left|\sigma_N\right|}, \tag{1}$$

where μ_s is the static coefficient of friction and μ_d is the dynamic coefficient of friction. The normal and tangential forces are calculated as

$$\begin{aligned} F_N &= P \cos^2 \beta \\ F_\tau &= P \cos \beta \sin \beta. \end{aligned} \tag{2}$$

Using equations 1 and 2, we obtain S independent of the pressure P only controlled by the friction properties and the angle β:

$$S = \frac{\mu_s \cos \beta - \sin \beta}{\sin \beta - \mu_d \cos \beta} \tag{3}$$

Andrews (1976) found for a homogeneous fault, that in dynamic rupture simulations supershear transitions are expected for $S < 1.7$. In Langer et al. (2012) we show that supershear transitions can occur for larger S at a bimaterial fault than at a homogeneous fault. In the next section we explain our model for the dynamic rupture propagation.

2.3. Dynamic rupture

To model a dynamic slip on a fault we adapt Gmsh to contain contact joint elements (Olsen-Kettle et al., 2008; Langer et al., 2010, 2012) in a way that is similar to the traction-at-split-node method (e.g. Andrews, 1999). We study numerical solutions of the 2D wave equation where the penalty method is used to enforce the contact boundary conditions (Perić and Owen, 1992; Laursen and Simo, 1993; Wriggers, 2006). The penalty method was also employed by Coker et al. (2005); Povirk and Needleman (1993) and Shi et al. (2008) in their implementation of elastoplasticity along homogeneous interfaces and in Olsen-Kettle et al. (2008); Langer et al. (2010) and Langer et al. (2012) along bimaterial interfaces. For the confined and horizontally unconfined configurations our simulations allow slip at the central 150 mm of the fault. For the fully unconfined configuration rupture is limited to the central 140 mm, as our model is 150 mm wide and faults have to be fully embedded in our model and can not touch the outer boundary.

2.4. Friction law

As in Langer et al. (2012) we are using the velocity-weakening friction law by Ampuero and Ben-Zion (2008). The friction coefficient along the fault is defined as

$$\mu_f = \mu_s + \alpha_{fr}\frac{V}{V+V_C} - \beta_{fr}\frac{\Theta}{\Theta+V_C}, \tag{4}$$

where V is the plastic slip-rate, μ_s is the static friction coefficient and α quantifies a rate (as in rate and state dependent friction laws) on the currently acting friction μ_f. The evolution effect β is a direct velocity strengthening mechanism with a regularizing effect (Ampuero and Ben-Zion, 2008). The dynamic friction coefficient can be calculated as $\mu_d = \mu_S + \alpha_{fr} - \beta_{fr}$. V_c is a characteristic velocity scale and τ_c is a characteristic time scale governing the evolution of the state variable Θ through $\dot{\Theta} = (V - \Theta)\,{\tau_C}^{-1}$. The characteristic slip-weakening distance is defined as $D_c \doteq V_c\,\tau_c$. Ranjith and Rice (2001) showed analytically that for a material pair with dissimilar elastic moduli frictional sliding is ill-posed. They propose regularization of the ill-posedness by introducing a fading memory to the normal stress. The numerical framework used in this paper incorporates an inherent general memory effect through the elastic response of the fault, as introduced by Olsen-Kettle et al. (2008) and also used in Langer et al. (2012). An elastic predictor, using a first order Taylor expansion, estimates the Coulomb failure stress at a future timestep by assuming first that the incremental displacement is purely elastic along the fault. If the estimated elastic failure stress is larger than zero, plastic yielding in the current timestep is initiated and calculated so that the Coulomb failure stress at the next timestep remains on the yield surface. This prevents physically invalid positive values of Coulomb failure stress. Since only the plastic slip-rate and not the total slip-rate is used in our friction law (see Eq. 4), the elastic component of the slip may provide

Table 2: Simulation parameters for dynamic rupture phase

Description	Parameter	Value
Maximum mesh grid step size	Δx [m]	$5 \cdot 10^{-4}$
Static Friction coefficient	μ_s	0.6
Direct effect coefficient	α_{fr}	0.001
Evolution effect coefficient	β_{fr}	0.401
Dynamic friction coefficient	$\mu_d = \mu_s + \alpha_{fr} - \beta_{fr}$	0.2
Slip-weakening distance	D_c [m]	$3.7 \cdot 10^{-6}$

a memory dependence through the elastic fault response. Olsen-Kettle et al. (2008) showed that this greatly reduces the mesh-dependency associated with the ill-posedness in the sense of Renardy (1992).

2.5. Rupture nucleation

The rupture nucleation mechanism is known to influence rupture propagation and supershear transition behavior (Festa and Vilotte, 2006; Shi et al., 2008; Lu et al., 2009). We therefore consider two different nucleation methods: In the first method (called the *numerical nucleation method*), we lower the static friction in the nucleation patch, so that the rupture is just initiated. However this means that for each simulation with different angle β and pressure P the static friction is lowered by a different amount. In the second method, the rupture is nucleated by introducing a defined stress drop in the nucleation patch. The overshoot of Coulomb failure stress changes when the direction of the principal stress or the amplitude of the applied pressure change. This might be an additional influence on the dynamic rupture propagation. We call this the *experimental nucleation method*, because it can be used as a model for the exploding wire mechanism (Xia, 2005), which is used in laboratory experiments. We tested both nucleation methods and found similar results, so we describe the experimental nucleation method in detail only in Appendix A.3, where we also show results for the experimental nucleation method. The numerical nucleation method follows Langer et al. (2012) and Ampuero and Ben-Zion (2008) where rupture is nucleated by setting the static friction in the nucleation site to a value of $\mu_s = |\tau| / |\sigma_N| - 0.001$. During the loading phase, the fault is still welded together by an infinitely high cohesion. To nucleate dynamic rupture, the cohesion is lowered to zero along the fault. In the nucleation patch, static friction is set to the lowered μ_s throughout the simulation. The advantage of this method is, that the nucleation itself is equal in its stress drop and overshoot for all simulations. One could argue that the influence of this type of nucleation on the rupture propagation does not differ between the various simulations. This is justified as the stress overshoot of 0.001 of the normal fault strength is similar for all simulations. In addition the following drop to dynamic stress by the acting friction

law with $\mu_d \geq 0$ is also similar for each simulation, independent of the fault inclination angle β and the Coulomb failure stress along the fault. So the nucleation mechanism should have a similar influence on the rupture propagation for all simulations, as the Coulomb stress 'overshoot' is comparable.

We choose our nucleation patch size of 7 mm in accordance with previous work (Lu et al., 2009), and we set the nucleation patch centered about the midpoint of the fault. When choosing larger values for the nucleation patch size, rupture occurs more readily and is more likely to be crack-like than pulse-like, as shown by Ampuero and Ben-Zion (2008). Much smaller values for the nucleation patch size results in no slip. An overview of model parameters for the friction law is shown in Table 2.

3. Investigating the influence of stress-distortions due to model setup on sub- and supershear rupture along bimaterial interfaces

The following sections present our results on the influence of stress-distortions present in the different bimaterial setups and their implications for interpretation of observed rupture processes. We start by presenting how the different model setups influence stress along the fault during static loading (section 3.1). Then we demonstrate that periodic boundary conditions are effective in eliminating distortions during loading (section 3.2). In section 3.3 we show the results of dynamic rupture propagation in simulations with the different loading schemes and compare the different supershear transition characteristics with those emerging from simulations with periodic boundary conditions without stress-distortions present. Lastly, in section 3.4 we show implications of stress-distortions for sub-Rayleigh rupture directivity.

3.1. Elastic deformation during far-field loading of a bimaterial fault

In Figure 2 we compare the normal and tangential stresses and Andrews' parameter S along the fault for the three model setups described in Figure 1. Figures 2a - 2c show that for all models, the tangential stresses along the fault are quite uniform, however, distinctive edge effects are apparent near the domain boundaries. The normal stresses in the confined configuration and horizontally unconfined configuration display significant variations along the fault caused by the presence of the platens which are either "welded" in the confined configuration or horizontally unconfined in the horizontally unconfined configuration. Because of the platens there is subsequent rotation in the model domain in the vicinity of the platen endpoints. In the fully unconfined configuration where platens are not present there are still edge effects present which lead to a significant normal stress edge effect near the interface only close to the model boundaries. However there the applied far-field shearing of the specimen shows as a counter clockwise bending in Figure 1c (with acute and obtuse specimen corners) due to dissimilar stiffnesses of the involved materials and leads to

distortion of the tangential stresses at the interface caused by the finite size of the model domain. Thus all configurations in Figure 1 display edge effects.

The differences between the model setups is most obvious in the normal stress-distributions. Both normal and tangential stresses display an expected dependence on the fault inclination angle β. The stress variations along fault, edge effects, dependence on fault inclination and the differences between model setups are all portrayed in the parameter S values along the fault (Figures 2d - 2f). In particular, the parameter S increases towards the direction of slip of the stiffer material, with values near the center of the fault matching the analytic values (except for the confined configuration which exhibits significantly higher values near the center). For all configurations the along-fault variation in S decreases with steeper angles β.

We note that all presented results of elastic deformation (Figure 2) are calculated assuming plane stress conditions. We repeat them for plane strain conditions as well and the graphs are qualitatively similar. Quantitatively, however, the deformations under plane strain conditions lead to distortions of the parameter S about three times larger than in plane stress conditions, as we show for one example in Figure A.1 in the appendix.

3.2. Periodic boundary conditions for distortion-free elastic deformation

Theoretically, increasing the model domain along the fault (in West-East direction) to an infinite size would result in a homogeneous stress-distribution along the bimaterial interface (i.e. it would eliminate the stress-distortions). While this is impossible in laboratory experiments (and the benefits of finite size increases are presented in the discussion), it is easily simulated numerically by implementing periodic boundary conditions at the borders perpendicular to the material interface (see Figure 3a, wavy lines). Figure 3a shows that there is no buckling of the specimen under the applied pressure. We record constant F_N, F_τ and Andrews' parameter S along the fault and no stress-distortions throughout the whole model domain. Figure 3b shows to what extent the fully unconfined configuration differs from the periodic configuration in parameter S. The values for F_N, F_τ and S in simulations with periodic boundary conditions are equal to their analytic counterparts. However there is a general disadvantage using periodic boundary conditions as the fault has to be aligned perpendicular to the model border so implementing complex fault geometry like bent faults is not possible. This limitation was highlighted in numerical work using the Discrete Element Method by Bardet and Proubet (1992) who showed that periodic boundary conditions prescribe shear plane directions and model a direct rather than a simple shear test. However they also state, that periodic boundary conditions prevent localized deformation patterns.

Using periodic boundary conditions does not necessarily simulate earth-like processes, as in-situ stress heterogeneities do influence rupture propagation and may even lead to supershear transitions (Wang and Mori, 2012). However periodic boundary conditions allow us to study the conditions for supershear transition isolated from the distorting influences of experimental setups.

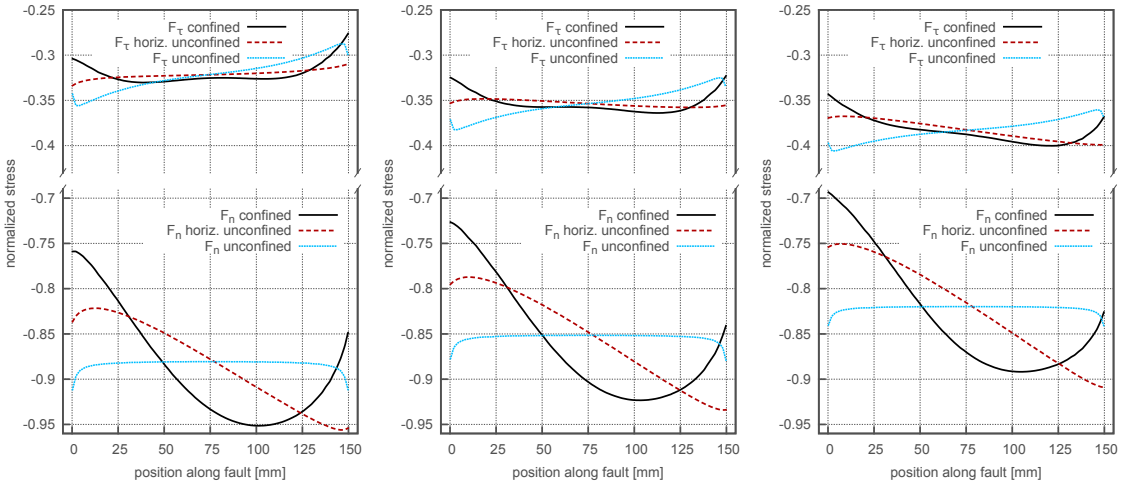

(a) Stresses along an interface with $\beta = 20°$

(b) Stresses along an interface with $\beta = 22.5°$

(c) Stresses along an interface with $\beta = 25°$

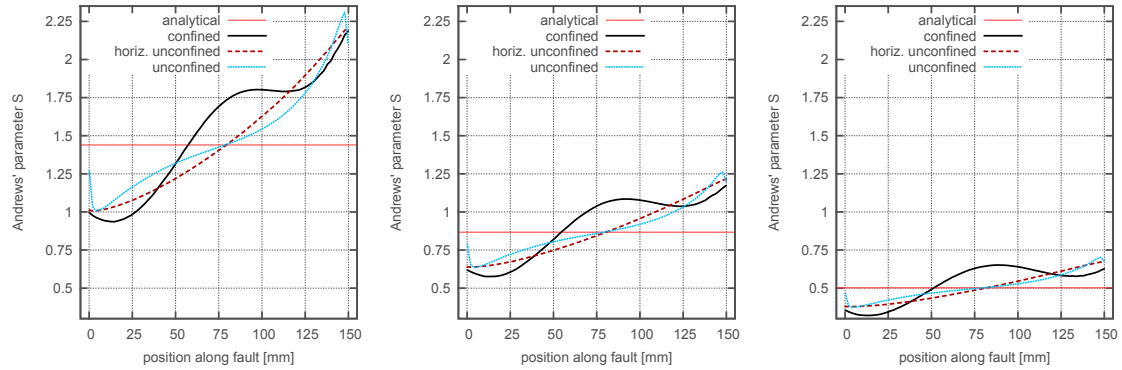

(d) Parameter S along an interface with $\beta = 20°$

(e) Parameter S along an interface with $\beta = 22.5°$

(f) Parameter S along an interface with $\beta = 25°$

Figure 2: (a)-(c) show the tangential and normal stresses along material interfaces in the three model setups (confined, horizontally confined and unconfined for $\beta = 20°, 22.5°, 25°$). The graphs show the current acting stresses at the fault divided by the absolute value of the applied pressure P, thus normalizing the stresses along the fault, but keeping their sign. Panels (d)-(f) show Andrews' parameter S along the faults in the three setups, assuming frictional values $\mu_s = 0.6$ and $\mu_d = 0.2$ (see Equation 1).

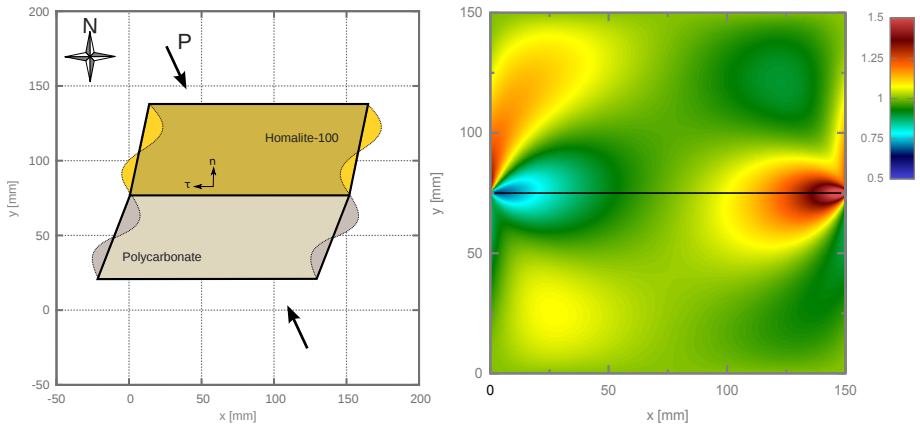

(a) Model region periodic (b) $S_{free}/S_{periodic}$

Figure 3: (a) Deformation patterns in a simulation of uniaxial compression test ($P = -10\,\mathrm{MPa}$, principal stress angle of 20°) with periodic boundary conditions applied along the Western & Eastern borders (the displacement is exaggerated 100 times). (b) The ratio between Andrews' parameter S in the fully unconfined configuration from Figure 1c (S_{free}) and the periodic configuration from panel a ($S_{periodic} = 1.439$), calculated over the entire model domain.

3.3. The effect of stress-distortions from model setup on supershear transitions

In nature rupture has been observed to transition from subshear to supershear speed (Bouchon and Vallée, 2003) and to propagate at intersonic velocities. Although earthquakes at supershear speeds are rare they yield higher ground motion than subshear earthquakes (Bernard and Baumont, 2005) so it is important to study them in the laboratory and in numerical models. In the former section we have seen, that different loading configurations induce differing stress-distortions. We demonstrate the implications of these distortions on rupture propagation and supershear transition length in order to improve the interpretation of numerical models and laboratory experiments.

We simulate dynamic rupture along a bimaterial interface using the three configurations outlined in Figure 1 and the periodic configuration shown in Figure 3a. We repeat our simulations for the range of fault orientations and applied a pressure P that is considered in recent lab experiments (Xia, 2005). The results for our parameter space study are shown in Table 3. Each cell shows the supershear transition length in the positive and in the negative direction as the upper and lower value respectively. The transition length is counted from the center of the fault, where the first 3.5 mm are within the nucleation patch. Where the rupture velocity stayed below the generalized Rayleigh wave speed until it reached the fault end, the cell entry is shown as '–'. Blank entries denote ruptures which either do not propagate beyond the nucleation patch or they decay (in the sense of Ampuero and Ben-Zion, 2008). We use a slip-weakening distance $D_c = 3.7\,\mu\mathrm{m}$ and the numerical nucleation method. The four configurations share common properties:

- Rupture propagation does not reach the end of the fault for low pressure P and low angle β.

In these conditions, ruptures do either not propagate beyond the nucleation patch or they decay (in the sense of Ampuero and Ben-Zion, 2008). In Table 3 this is shown as a blank entry.

- With increasing pressure P or an increasing angle β the occurrence of a supershear transition becomes more likely. The supershear transition length decreases with increasing pressure P and increasing parameter β (as implied by Rosakis et al. (2007), eq. 3.3.2).

- The supershear transition length in the positive direction is always equal to or larger than that in the negative direction. We have shown this also in Langer et al. (2012). This is caused by the bimaterial effect which alters the Coulomb failure stress ahead of the crack tip, delaying or promoting the supershear transition (in the positive and negative direction, respectively).

- For the largest P and β examined here, the supershear transition length is below 10 mm – it takes place shortly after leaving the nucleation patch. With decreasing P or β the transition length increases, however the values in Table 3 seem to 'jump' the range between 10 mm and 20 mm, which suggests that a direct supershear transition mode may be present. Immediate supershear transition in the negative direction has also been found by Xia et al. (2005) for $\beta = 25°$and $P = 18$ MPa. Numerical studies have also shown that for a strongly loaded nucleation zone one "... can make the main crack transition to intersonic speeds right outside the nucleation zone." (Liu and Lapusta, 2008, p. 43). The numerical nucleation method used here deploys a stress drop $\Delta\sigma_N = \mu_s\sigma_N - \tau/\sigma_N$ in the nucleation patch to initiate rupture. From equation 2 we find $\Delta\sigma_N \propto P$, thus the nucleation zone is loaded stronger for higher P than for lower ones. Additionally, as a higher angle β causes a lower S (see equation 3), the change into the mode of immediate supershear transition is promoted. Immediate supershear transition in the negative direction has also been found by Xia et al. (2005) for $\beta = 25°$and $P = 18$ MPa.

The supershear transition lengths for the four model configurations differ in a qualitative way:

- The horizontally confined, the unconfined and the periodic model configurations show similar transition lengths for large β. For large β, transition lengths are generally short and the S distribution around the nucleation site is quite similar at approximately equal to the analytical value for S at these locations. For the confined configuration, the parameter S is higher around the nucleation site than for other three configurations as seen in Figure 2. The effect is, that the supershear transition occurs later towards the fault end, where the value of S is lower than in the other configurations. Immediate supershear transitions are less prevalent for higher S as can be seen in all configurations. Therefore transition right

outside the nucleation patch occurs only for higher β in the confined configuration than in other configurations. This may partially explain why experiments by Xia (2005) have not observed supershear transitions in the positive direction as the transition lengths in general are longer for the confined configuration and for the positive direction they are always longer than the negative direction.

- For the confined configuration supershear transitions are more likely to occur in both rupture directions due to very low S in the positive direction towards the fault ends. However because the S-value is lowered towards the end of the fault it leads to longer transition lengths possibly making the transition in the positive direction harder to observe experimentally.

- The horizontally unconfined configuration and the fully unconfined configuration are very similar in their transition lengths due to their very similar distribution of the parameter S.

- Ruptures in the periodic configuration transition in the negative direction for smaller angles β than in the other three configurations, as its parameter S in the negative direction in lower than in the other configurations.

- Apart from immediate supershear transitions influenced by the nucleation, there are no supershear transitions in the positive direction for the periodic configuration for $\beta < 25°$and $P < 13\,\mathrm{MPa}$. This is similar to the experiments by Xia (2005) where they did not observe any supershear transitions in the positive direction.

Table 3 clearly shows that the supershear transition is affected by experimental and numerical setups. For periodic configurations without stress-distortions one should expect subshear propagation in the positive direction and supershear in the negative direction for a much wider P-β-parameter space than in laboratory experiments as confirmed by this table. The laboratory experiments by Xia (2005) were conducted with $\beta = 20°$, $22.5°$, $25°$. They reported supershear transitions exclusively in the negative direction, and in this aspect their results match best with the periodic configuration in Table 3. However another possibility for the absence of supershear transitions in the positive direction could be that using a confined configuration in their experiments leads to longer transition lengths in the positive direction which may have been outside the observational range. It is possible to closely match the results of Xia (2005) by manipulating the parameters of the friction law. Table A.3 in the appendix shows, that with $\mu_s = 0.63$ and $D_c = 5\,\mu\mathrm{m}$ results for all configurations are similar to their experiments. We conduct a number of parameter sweeps altering friction properties. For all the tested ranges of parameters the loading configuration influences the occurrence of supershear transition and transition lengths as described in Appendix A.2.

	Confined								Horizontally unconfined								Fully unconfined								Periodic							
°\MPa	10	11	12	13	14	15	16	17	10	11	12	13	14	15	16	17	10	11	12	13	14	15	16	17	10	11	12	13	14	15	16	17
20.0						–	–	–				–	–	–	–	–				–	–	–	–	–				–	–	–	–	–
						–	–	–				–	–	–	–	–				–	–	–	–	–				–	–	–	–	–
20.5				–	–	–	–	–			–	–	–	–	–	–			–	–	–	–	–	–			–	–	–	–	–	–
					–	–	–	–			–	–	–	–	–	–			–	–	–	–	–	–			–	–	–	–	–	–
21.0			–	–	–	–	–	–	–	–	–	–	–	–	–	–		–	–	–	–	–	–	–		–	–	–	–	–	–	–
			–	–	–	–	–	–		–	–	–	–	–	–	–		–	–	–	–	–	–	–		–	–	–	63	56	46	42
21.5		–	–	–	–	–	–	–	–	–	–	–	–	–	–	–	–	–	–	–	–	–	–	–	–	–	–	–	–	–	–	–
		–	–	–	–	–	–	–	–	–	–	–	–	–	–	–	–	–	–	–	–	–	–	–	–	63	53	45	41	37	35	32
22.0	–	–	–	–	–	–	–	–	–	–	–	–	–	–	–	–	–	–	–	–	–	–	–	–	–	–	–	–	–	–	–	–
	–	–	–	–	43	42	38	38	–	–	–	–	–	–	50	38	–	–	–	–	45	38	32	27	51	43	37	34	31	28	27	20
22.5	–	–	–	–	–	–	–	–	–	–	–	–	–	–	–	–	–	–	–	–	–	–	–	–	–	–	–	–	–	–	–	–
	–	56	42	37	36	32	32	29	–	–	43	39	32	27	8	7	–	47	37	32	27	23	7	7	37	32	30	27	23	18	7	7
23.0	–	–	–	–	–	–	–	71	–	–	–	–	–	–	–	9	–	–	–	–	–	–	–	–	–	–	–	–	–	–	–	–
	41	37	34	31	30	27	25	8	45	34	30	23	7	7	7	7	34	31	26	22	8	7	7	6	28	26	22	19	7	7	6	6
23.5	–	70	68	67	59	56	52	51	–	–	–	72	71	73	8	7	–	–	–	–	–	–	12	7	–	–	–	–	–	–	7	9
	33	30	28	26	22	8	7	7	28	24	17	7	7	6	6	6	26	22	9	7	7	6	6	6	23	19	8	7	7	6	6	6
24.0	65	53	52	49	45	45	41	15	71	60	53	46	8	7	6	6	–	–	–	–	63	7	7	6	–	–	–	–	–	7	7	6
	28	24	22	16	7	7	7	6	21	8	7	6	6	6	6	6	19	8	7	6	6	6	6	6	18	7	7	6	6	6	6	6
24.5	48	45	41	38	35	8	7	7	45	36	8	7	7	6	6	6	64	54	44	7	7	6	6	6	–	–	–	9	7	6	6	6
	23	20	7	7	6	6	6	6	8	7	6	6	6	6	5	5	8	7	6	6	6	6	5	5	8	7	6	6	6	6	5	5
25.0	38	34	31	11	7	7	6	6	18	7	7	6	6	6	5	5	37	8	7	6	6	6	6	5	68	22	7	6	6	6	6	6
	18	7	7	6	6	6	6	5	7	6	6	6	5	5	5	5	7	6	6	6	5	5	5	5	7	6	6	6	5	5	5	5

Table 3: Supershear transition lengths in millimeters from the center of the nucleation patch for slip-weakening distance $D_c = 3.7\,\mu$m. Each cell contains the supershear transition length in the westward (positive) direction as the upper value and in the eastward (negative) direction as the lower value. Rupture does not reach the fault end for empty entries, it reaches the end without a supershear transition for '–'.

We also repeat the numerical simulations with the experimental nucleation method, yielding qualitatively similar results to Table 3. We show them in Table A.4 in the appendix. We also explore, how sensitive the supershear transition length is to a change in static and dynamic friction and found, that lowering μ_s and μ_d, but keeping a constant stress drop f_s had a similar effect as lowering D_c (see Tables A.3 for the numerical nucleation method, A.5 for the experimental nucleation method).

3.4. Implications for rupture mode and directivity of sub-Rayleigh ruptures

As shown in Figure 2d-f, the fully unconfined configuration displays stress-distortions smaller than the confined models. Therefore we chose to conduct a case study comparing rupture directivity and the occurrence of pulse-like and crack-like rupture for the fully unconfined configuration and the periodic configuration. Thus any emerging differences in rupture characteristics would also be good indicators of greater distortion-induced features in the confined and in the horizontally unconfined configurations.

To carefully evaluate differences in rupture properties such as potency or slip velocities, we use simulations with larger domain size (650 x 350 mm) and a fault that is twice as long (300 mm) as for the simulations in the previous sections. This would enable us to better decide if the rupture mode is pulse-like or crack-like (assuring that pulse width at any time is small compared to the

total fault length). The larger domain size here and the observed fault segment extending less than half the length of the domain also mean that the stress-distortion at the fault are smaller than in the previous section.

A far-field normal stress of -11.6 MPa and a far-field tangential stress of -4.03 MPa are applied, which could also be expressed as $P = -13\,\mathrm{MPa}$ and $\beta = 19.2°$. This angle is chosen here to obtain $S = 1.7$ and thus to avoid supershear transition (Andrews, 1976). We sweep over a range of characteristic velocity and time scales (V_c and τ_c) of the friction law (Equation 4) to capture a wide range of fault rupture behavior. We set $D_c \doteq V_c \tau_c$ with a fixed $D_c = 4.7\,\mu\mathrm{m}$. Lower values of V_c result in cracks and higher values of V_c lead to sustained or decaying pulses which enables us to explore a wider range of rupture modes (Ampuero and Ben-Zion, 2008). With 400 rupture propagation simulations we sweep over the parameter V_c of the friction law for values between 0.14 m/s and 0.24 m/s in 200 steps for the fully unconfined configuration and the periodic configuration.

We classify the ruptures as:

Cracks , when at least 75% of the fault is slipping at the same time for at least one time step of our model run (as in Figure 4c),

Bilateral pulses , when the rupture reaches both fault ends, but at no time more than 75% of the fault slips (as in Figure 4b, periodic configuration),

Unilateral pulses , where only one pulse reaches the fault end and the rupture stops in the other direction before reaching the fault end (as in Figure 4a for fully unconfined configuration), and

Decaying pulses , when neither end of the fault is reached.

For the lower values of V_c the rupture will be crack-like. With an increasing V_c the rupture changes to become sustained pulse-like, then decaying pulse-like and for the highest values of V_c rupture will not propagate and stays within the nucleation site.

To determine the effect of the boundary conditions we compare slip-profiles in Figure 4. We choose ruptures with a similar potency (Heaton and Heaton, 1989) in the westward direction and compare their eastward potency. Figures 4a and 4b show pulse-like ruptures. We observe that for the periodic configuration the difference in potency between the Western and Eastern half of the fault is smaller than for the fully unconfined configuration. This demonstrates that stress-distortions in non-periodic configurations affect rupture directivity. With the fully unconfined configuration the non-uniform parameter S enhances the effect of rupture directivity along bimaterial faults (Figure 4a). This may lead to misleading experimental results where the effect of the parameter S amplifies the effect of rupture directivity at bimaterial interfaces.

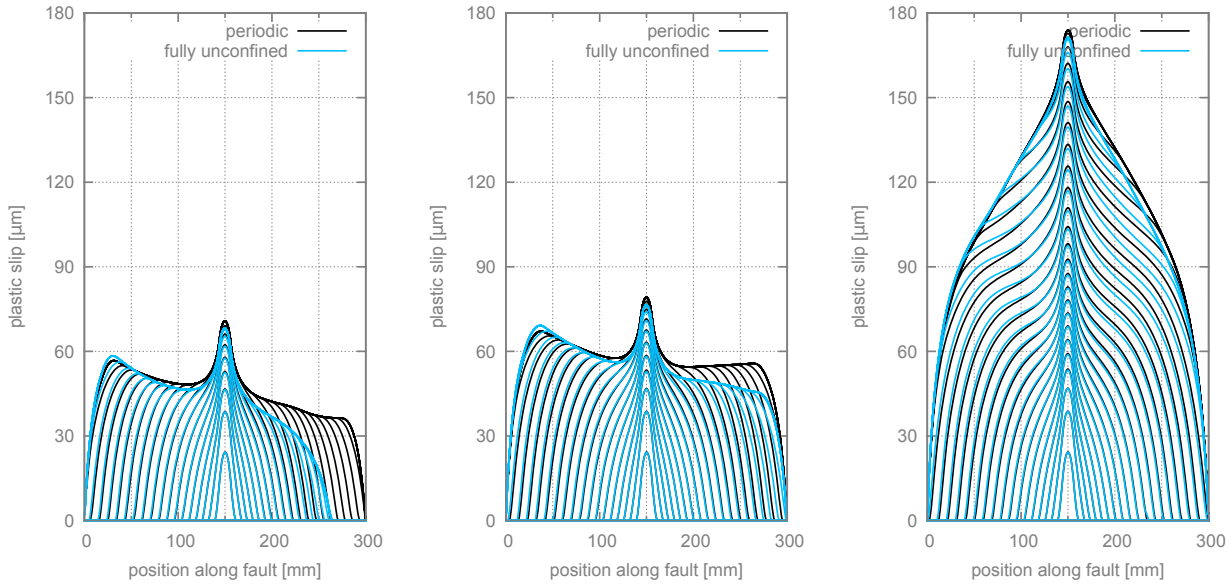

(a) (b) (c)

Figure 4: Comparison of slip profiles with similar westward potency, Figure 4c shows crack-like rupture, Figure 4b shows a bilateral pulse-like rupture and Figure 4a a bilateral pulse-like rupture for periodic boundary conditions and a unilateral pulse-like rupture for unconfined boundary conditions. The westward direction is the direction of rupture of the slower and more compliant material, Polycarbonate.

We also see in Figure 4a that the influence of stress-distortions is strong enough to lead to a unilateral pulse for a fully unconfined configuration, whereas the rupture is a bilateral pulse for the periodic configuration. However, if the fault had been longer in the periodic configuration, the rupture would eventually have stopped as well (because the rupture is a slowly decaying pulse in the negative direction). This is contrasted by Figure 4b where both rupture modes are bilateral pulses. However for a much longer fault, rupture would eventually have stopped in the eastward (negative) direction for the fully unconfined configuration as the pulse is decaying slowly in this direction. Table A.1 shows the dynamic rupture properties in detail. In a statistical overview we examine all 400 rupture propagations for their rupture mode to quantitatively determine the difference in rupture directivity between the fully unconfined configuration and the periodic configuration. As cracks always rupture bilaterally and decaying pulses do not fully rupture in any direction, we are interested only in bilateral and unilateral pulses. Table 4 shows 69% (25 of 36) of all pulses being unilateral for the fully unconfined configuration, whereas for the periodic configuration 53% (16 of 30) are unilateral. This suggests an overestimation of the occurrence of unilateral pulses in bimaterial ruptures if stress-distortions are presents.

For crack-like ruptures we find a higher potency in the westward (positive) direction for the fully unconfined configuration, but a higher potency for eastward (negative) rupture for the periodic configuration. There are two competing effects during crack-like rupture. When crack-like rupture occurs at a point on the fault that point continues slipping during the entire rupture event until the rupture has reached the end of the fault and the backward healing phase has arrived to heal it. So for the westward rupture, which is the positive direction, the rupture velocity is faster in this direction and the backward healing phase arrives sooner for this westward direction than the slower eastward rupture. This can lead to an unexpected result for the periodic configuration where the westward rupture has healed faster for the positive direction leading to a smaller potency in this direction than in the negative direction. However for the fully unconfined configuration the effect of the lowered parameter S in the positive direction leads to higher slips and larger potencies despite earlier arrest.

We conduct the simulations here for the fully unconfined configuration which has the smallest stress-distortions of the three models without periodic boundary conditions. Simulations and experiments with the other two non-periodic boundary conditions shown in Figure 1 (a) and (b) would show more dependence of rupture characteristics on experimental or model setup.

4. Discussion

We summarize the source of the stress heterogeneities (section 4.1), next we show implications for rupture properties in laboratory experiments and numerical simulations (section 4.2) and lastly we try to set our results in the broader context of processes in past laboratory experiments (section

Table 4: Rupture modes compared for non-periodic and periodic boundary conditions

Boundary condition	Cracks	Bilateral pulses p_b	Unilateral pulses p_u	Decaying pulses	pulse ratio $p_u/(p_u+p_b)$
Non-periodic	68	11	25	96	0.69
Periodic	62	14	16	108	0.53

4.3).

4.1. The source of the stress heterogeneities

We conduct Finite Element simulations of dynamic rupture along faults embedded between Homalite-100 and Polycarbonate, using four different loading configurations. The confined configuration represents a laboratory experiment setup used in recent experiments to determine properties of dynamic rupture (Xia et al., 2005) where a specimen is subjected to a uniaxial compression test. The top and bottom model boundaries represent platens of a hydraulic press and are displaced to load the specimen from afar. Movement between the specimen and the platens is suppressed by confinement. The horizontally unconfined configuration represents an alternative configuration for laboratory experiments, where a 'friction reducer' is used to lubricate the contact surface between the platens and the specimen. In our model we represent this by allowing tangential motion along the top and bottom boundaries. The fully unconfined configuration represents a model setup typical of numerical simulations of dynamic rupture (Harris and Day, 1997; Andrews and Ben-Zion, 1997; Shi and Ben-Zion, 2006; Langer et al., 2010) with far-field loading at the model boundaries. Finally, the periodic configuration has periodic boundaries perpendicular to the orientation of the fault.

The model domain is loaded with different pressure P and the angle β between the principal stress and the fault is varied. Since the elastic moduli of our two materials are not equal, the differing Poisson's ratios lead to differing strains near the material interface, which introduce shearing and a change in normal and tangential stresses along the fault. In the confined configuration an additional distortion of the stress field is present along the top and bottom boundaries, where a Poisson's ratio of zero is imposed (forming a material contrast greater than around the fault).

In section 3.2 we find that the stress-distortion along interfaces can be avoided in numerical models by implementing periodic boundary conditions. Simulations with the periodic configuration exhibit a constant S along the material interface, equal to the analytically predicted value. While periodic boundary conditions are not suitable for all models (e.g. simple shear tests by Bardet and Proubet, 1992), they could improve models with prescribed shear planes perpendicular to the periodic boundary (e.g. Cundall, 1989). Modeling rupture on complex fault geometries includ-

ing branches and bends is also not feasible with periodic boundaries, but nevertheless, multiple bimaterial interfaces oriented parallel to faults can be implemented (Harris and Day, 1993).

Finally, not all laboratory experiments and numerical models are influenced by the stress-distortions found here. Studies of rupture along homogeneous interfaces (Andrews, 1976; Harris and Day, 1993; Coker et al., 2005; Liu and Lapusta, 2008; Lu et al., 2009) are not affected by the stress-distortions described in this paper, as long as they do not employ horizontally confined boundaries (which practically introduce a material interface at the edge of the model). Likewise simulations with bimaterials are not affected, if the fault separates two semi-infinite half-spaces as in Cochard and Rice (2000). However, most studies with rupture along bimaterial interfaces are affected when preloading is applied at the boundaries (Harris and Day, 1997; Andrews and Ben-Zion, 1997; Shi and Ben-Zion, 2006; Langer et al., 2010). The dissimilar stiffness matrices of the two materials involved lead to a bending effect towards the edges of the model. Laboratory setups with impact loading (Coker et al., 2005; Lambros and Rosakis, 1994; Rosakis et al., 1998) and other experiments without preloading prior to nucleation are not affected by this distortion.

4.2. Implications for rupture characteristics observed in laboratory experiments and numerical simulations

In sections 3.3 and 3.4 we conduct dynamic rupture simulations using the four model configurations presented above. The stress patterns induced by static loading have a significant effect on the dynamic rupture characteristics. We closely examine the differences in supershear transition length between the four models. As the normal and tangential stress along the fault vary, Andrews' parameter S changes along the fault, which alters the supershear transition length. We demonstrate that the four loading configurations differ in their transition length. For the confined configuration we obtain supershear transitions in the negative direction, but also a promotion of a supershear transition in the positive direction by a lowered parameter S towards the positive fault end (see Figure 2 for S distribution and Table 3 for transition lengths). The fully unconfined configuration and the horizontally unconfined configuration are quite similar in their distortions along the fault and also in their supershear transitions. Excluding conditions of high P and high β (where a strongly loaded nucleation promotes immediate supershear transitions as seen by Liu and Lapusta, 2008), the periodic configuration shows no supershear transition in the positive direction and transitions in the negative direction for lower angles β than the other configurations.

We then evaluate the influence of distorted fault stresses on properties of dynamic ruptures at sub-Rayleigh speeds. We compare rupture characteristics in simulations of the (undistorted) periodic configuration with those of the fully unconfined configuration which displays the smallest distortions of all the non-periodic configurations (Figure 2d-f). For all simulations in both configurations, we found that subshear rupture speeds are higher in the positive direction. Unilateral rupture exclusively occurs for pulses, however there are also bilateral pulses. Cracks are always

bilateral in agreement with Rubin and Ampuero (2007). Pulse-like ruptures in the positive direction display larger rupture lengths, higher velocities and higher potency for the fully unconfined configuration than for the periodic configuration. Stress-distortions also influence rupture directivity (i.e. whether a rupture is bilateral or unilateral). We show that for the fully unconfined configuration unilateral ruptures occur more often than for the periodic configuration. Unilateral rupture occurs always in the positive direction. Where the rupture would have arrested before the fault end in the positive direction for a periodic configuration, it is promoted due to a lowered S in a fully unconfined configuration (e.g. see distribution of S in Figure 2e). In some of the cases where crack-like rupture occurred, the potency in the negative direction was found to be larger than in the positive direction. This is because a higher rupture speed in the positive direction means that the crack-tip reaches the fault-end earlier and the backward healing phase arresting rupture propagates backwards from the fault-end earlier than in the negative direction, leading to a lower potency (see Figure 4c). This is not the case for pulses where rupture arrest occurs directly after the pulse has passed through a fault segment. For pulses the potency and rupture velocity are found to be always higher in the positive rupture direction.

4.3. Implications for interpretation of laboratory experiments

The stress-distortion along a material interface results from far-field application of stresses at the model boundary. In finite-size models, the strains across the interface are largest at the edge of the specimen (where the interface reaches the free surface). We therefore conducted additional simulations with a range of larger domain sizes to evaluate how the proximity of the fault to the specimen edge affects the stress-distortions. Figure 5 shows the effect of a larger specimen size on the stress levels (parameter S) in our three non-periodic model configurations. Using larger model domains significantly reduces the edge effects and associated stress-distortions along the faults. Where possible, laboratory experiments should therefore be redesigned to maximize the distance between ruptures and free-surfaces. Alternatively, rupture observations should be acquired far from the edges where the effect of stress-distortions is not dominant and can be evaluated. This would allow laboratory experiments to provide even more accurate insights into real-world rupture phenomena. It is also important to note a quantitative difference between the model configurations. For the unconfined configurations (Figures 5b, 5c), parameter S at the fault mid-point (75 mm) nears the analytical value, whereas in the confined configuration (Figure 5a) the S-value in the center is much higher in all simulations (regardless of domain size). In order to estimate the transition length in a confined configuration experiment (as in Rosakis et al. (2007), eq. 3.3.2), one would therefore have to consider this deviation from analytical S-values.

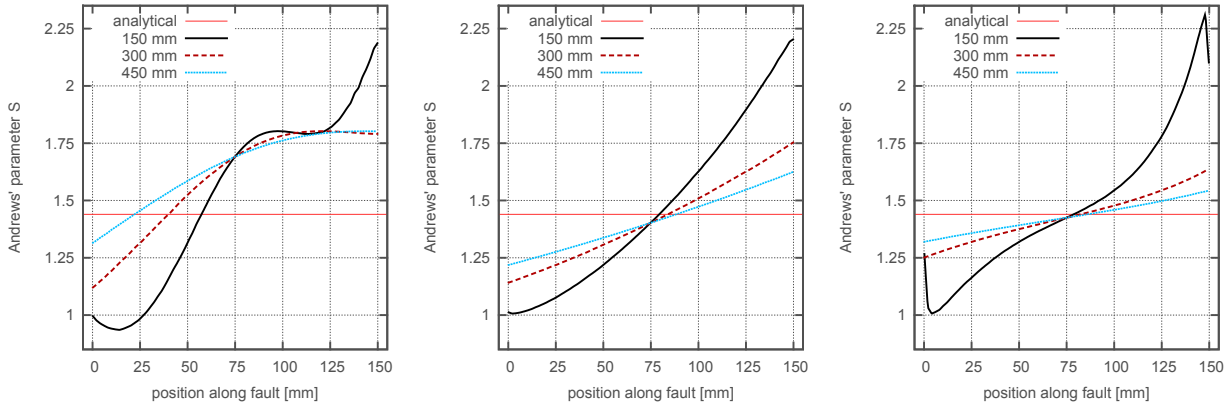

(a) confined configuration (b) horizontally unconfined configuration (c) fully unconfined configuration

Figure 5: The distribution of parameter S along faults (150 mm long) embedded in models of 150 mm, 300 mm and 450 mm boundary length. The stress-distortions near the fault tips are much smaller in simulations with large model domains (where the fault is far from the free surface).

4.4. The effect of localized friction variations along faults

Our results show that the supershear transitions demonstrated by the experiments of Xia et al. (2005) could be reproduced by our work by all of the configurations by varying different parameters of the friction law. Generally we observe in section 3.3 that the periodic and confined configurations match the supershear transitions for a P, β-pair in the laboratory experiments best. Future laboratory experiments such as those presented by Xia et al. (2005) could be extended to examine the influence of configuration-induced stress-distortions on rupture behavior. This could be achieved by using larger specimen sizes to quantify the extent that stress-distortions in their experimental setup affects rupture behavior by comparing with in Figure 5.

Future work could also investigate other factors which may be present. Recent slider block experiments Ben-David and Fineberg (2011) found that stress-distortions along faults led to heterogeneous micro-slip and they showed this greatly affects rupture nucleation and propagation. Furthermore, Ben-David et al. (2010) indicated that local stress peaks along such interfaces may be several times higher than the bulk shear strength of the material. Further research could be conducted to observe if contact surfaces are slipping and relaxing the fault at the μm-scale as described by Rubinstein et al. (2006).

In future numerical work it would be interesting to use a fractal distribution of the coefficient of friction along the interface to model the non-uniform stresses. We might expect that small pre-nucleation slip-events would occur near the positive fault end in our three non-uniform loading configurations, where the ratio of tangential to normal stresses is large. This would relax peak stresses and prevent supershear transitions in the positive direction. Relaxation of a fault by μm-

scale slipping could partially contribute to the findings of Lu et al. (2009), that their numerical models with a homogeneous material had 30 to 40 percent shorter supershear transition lengths than the laboratory experiments by Xia et al. (2004).

5. Conclusion

In numerical modeling and laboratory experiments the distortion of a bimaterial specimen as a response to loading can be eliminated by increasing specimen size in laboratory experiments or by applying periodic boundary conditions to a numerical model. Simulations using non-periodic boundary conditions are capable of modeling laboratory experiments whereas periodic boundary conditions are more appropriate for studies of rupture propagation in a geophysical context. When loaded at its boundaries, a model with non-periodic boundary conditions shows larger rupture directivity than a model with periodic boundaries in case of sub-Rayleigh velocity rupture propagation. The occurrence of supershear transition and the transition lengths strongly depend on model setup.

Acknowledgements

We thank Hans Mühlhaus, Yehuda Ben-Zion and Aurélie Papon for discussions and suggestions. This research is supported by The University of Queensland, the Australian Research Council Linkage project LP0562686 with the Queensland Department of Main Roads and The University of Queensland, and AuScope Ltd which is funded under the National Collaborative Research Infrastructure Strategy (NCRIS) an Australian Commonwealth Government Programme. Software was developed by the Australian Computational Earth Systems Simulator Major National Research Facility and computations were performed on the Australian Earth Systems Simulator, an SGI ICE 8200 EX supercomputer.

References

Adams, G. G., 2001. An intersonic slip pulse at a frictional interface between dissimilar materials. Journal of Applied Mechanics 68 (1), 81–86.

Ampuero, J.-P., Ben-Zion, Y., 2008. Cracks, pulses and macroscopic asymmetry of dynamic rupture on a bimaterial interface with velocity-weakening friction. Geophys. J. Int. 173 (2), 674–692.

Anderson, P. W., 1972. More is different. Science 177 (4047), 393–396.

Andrews, D. J., nov 1976. Rupture velocity of plane strain shear cracks. J. Geophys. Res. 81 (32), 5679–5687.

Andrews, D. J., 1999. Test of two methods for faulting in finite difference calculations. Bull. Seismol. Soc. Am. 89, 931–937.

Andrews, D. J., Ben-Zion, Y., 1997. Wrinkle-like slip pulse on a fault between different materials. J. Geophys. Res. 102, 553–571.

Bardet, J., Proubet, J., 1992. Numerical simulations of shear bands in idealized granular materials. Solid State Phenomena 23-24, 473–481.

Ben-David, O., Cohen, G., Fineberg, J., 2010. The dynamics of the onset of frictional slip. Science 330 (6001), 211–214.

Ben-David, O., Fineberg, J., Jun 2011. Static friction coefficient is not a material constant. Phys. Rev. Lett. 106 (25), 254301.

Ben-Zion, Y., 2001. Dynamic ruptures in recent models of earthquake faults. J. Mech. Phys. Solids 49, 2209–2244.

Bernard, P., Baumont, D., 2005. Shear mach wave characterization for kinematic fault rupture models with constant supershear rupture velocity. Geophys. J. Int. 162 (2), 431–447.

Bhat, H. S., Biegel, R. L., Rosakis, A. J., Sammis, C. G., 2010. The effect of asymmetric damage on dynamic shear rupture propagation ii: With mismatch in bulk elasticity. Tectonophysics 493 (3-4), 263–271.

Biegel, R. L., Bhat, H. S., Sammis, C. G., Rosakis, A. J., oct 2010. The effect of asymmetric damage on dynamic shear rupture propagation i: No mismatch in bulk elasticity. Tectonophysics 493 (3-4), 254–262.

Bouchon, M., Vallée, M., 2003. Observation of long supershear rupture during the magnitude 8.1 kunlunshan earthquake. Science 301 (5634), 824–826.

Burridge, R., 1973. Admissible speeds for plane-strain self-similar shear cracks with friction but lacking cohesion. Geophys. J. R. astr. Soc. 35 (4), 439–455.

Byerlee, J., 1978. Friction of rocks. Pure Appl. Geophys. 116 (4), 615–626.

Cochard, A., Rice, J. R., 2000. Fault rupture between dissimilar materials: Ill-posedness, regularization, and slip-pulse response. J. Geophys. Res. 105 (B11), 25,891–25,907.

Coker, D., Lykotrafitis, G., Needleman, A., Rosakis, A., 2005. Frictional sliding modes along an interface between identical elastic plates subject to shear impact loading. J. Mech. Phys. Solids 53 (4), 884–922.

Cundall, P. A., 1989. Numerical experiments on localization in frictional materials. Archive of Applied Mechanics 59 (2), 148–159.

Dunham, E. M., Archuleta, R. J., 2004. Evidence for a supershear transient during the 2002 denali fault earthquake. Bull. Seismol. Soc. Am. 94 (6B), S256–S268.

Festa, G., Vilotte, J. P., 2006. Influence of the rupture initiation on the intersonic transition: Crack-like versus pulse-like modes. Geophys. Res. Lett. 33, L15320.

Geuzaine, C., Remacle, J.-F., 2009. Gmsh: A 3-d finite element mesh generator with built-in pre- and post-processing facilities. Int. J. Numer. Meth. Eng. 79 (11), 1309–1331.

Gross, L., Bourgouin, L., Hale, A. J., Muhlhaus, H. B., Aug. 2007. Interface modeling in incompressible media using level sets in escript. Physics of the Earth and Planetary Interiors 163, 23–34.

Harris, R. A., Day, S. M., 1993. Dynamics of fault interaction: Parallel strike-slip faults. J. Geophys. Res. 98 (B3),

4461–4472.

Harris, R. A., Day, S. M., 1997. Effects of a low-velocity zone on a dynamic rupture. Bull. Seismol. Soc. Am. 87, 1267–1280.

Heaton, T. H., Heaton, R. E., 1989. Static deformations from point forces and force couples located in welded elastic poissonian half-spaces: Implications for seismic moment tensors. Bull. Seismol. Soc. Am. 79 (3), 813–841.

Labuz, J. F., Dai, S. T., Papamichos, E., 1996. Plane-strain compression of rock-like materials. International Journal of Rock Mechanics and Mining Sciences & Geomechanics Abstracts 33 (6), 573–584.

Lambros, J., Rosakis, A. J., feb 1994. Dynamic decohesion of bimaterials: Experimental observations and failure criteria. NASA STI/Recon Technical Report N 95, 18613.

Langer, S., Olsen-Kettle, L., Weatherley, D., 2012. Identification of supershear transition mechanisms due to material contrast at bimaterial faults. Geophys. J. Int. 190 (2), 1169–1180.

Langer, S., Olsen-Kettle, L. M., Weatherley, D. K., Gross, L., Mühlhaus, H.-B., 2010. Numerical studies of quasi-static tectonic loading and dynamic rupture of bi-material interfaces. Concurrency Computat. Pract. Exper. 22 (12), 1684 – 1702.

Laursen, T. A., Simo, J. C., 1993. A continuum-based finite element formulation for the implicit solution of multi-body large deformation frictional contact problems. Int. J. Numer. Meth. Eng. 36, 3451–3485.

Liu, Y., Lapusta, N., 2008. Transition of mode ii cracks from sub-rayleigh to intersonic speeds in the presence of favorable heterogeneity. Journal of the Mechanics and Physics of Solids 56 (1), 25–50.

Lu, X., Lapusta, N., Rosakis, A. J., 2009. Analysis of supershear transition regimes in rupture experiments: the effect of nucleation conditions and friction parameters. Geophys. J. Int. 177 (2), 717–732.

Ohnaka, M., 2003. A constitutive scaling law and a unified comprehension for frictional slip failure, shear fracture of intact rock, and earthquake rupture. J. Geophys. Res. 108 (2080), 10–1029.

Olsen-Kettle, L. M., Weatherley, D., Saez, E., Gross, L., Mühlhaus, H. B., Xing, H. L., 2008. Analysis of slip-weakening frictional laws with static restrengthening and their implications on the scaling, asymmetry, and mode of dynamic rupture on homogeneous and bimaterial interfaces. J. Geophys. Res. 113, B08307.

Perić, D., Owen, D. R. J., 1992. Computational model for 3-d contact problems with friction based on the penalty method. Int. J. Numer. Meth. Eng. 35, 1289–1309.

Povirk, G. L., Needleman, A., 1993. Finite element simulations of fiber pull-out. Journal of Engineering Materials and Technology 115, 286–291.

Ranjith, K., Rice, J. R., 2001. Slip dynamics at an interface between dissimilar materials. J. Mech. Phys. Solids 49, 341–361.

Ravi-Chandar, K., 2004. Dynamic fracture. Elsevier Science.

Ravi-Chandar, K., Knauss, W. G., 1984. An experimental investigation into dynamic fracture: Ii. microstructural aspects. International Journal of Fracture 26 (1), 65–80, 10.1007/BF01152313.

Rayleigh, J. W. S., 1885. On waves propagated along the plane surface of an elastic solid. Proc. London Math. Soc. 17 (1), 4–11.

Renardy, M., 1992. Ill-posedness at the boundary for elastic solids sliding under coulomb friction. Journal of Elasticity 27 (3), 281–287.

Rosakis, A., Samudrala, O., Singh, R., Shukla, A., 1998. Intersonic crack propagation in bimaterial systems. J. Mech. Phys. Solids 46 (10), 1789–1814.

Rosakis, A. J., Xia, K., Lykotrafitis, G., Kanamori, H., 2007. Dynamic shear rupture in frictional interfaces: Speeds, directionality, and modes. In: Schubert, G. (Ed.), Treatise on Geophysics. Elsevier, Amsterdam, pp. 153–192.

Rubin, A. M., Ampuero, J.-P., 2007. Aftershock asymmetry on a bimaterial interface. J. Geophys. Res. 112, 0148–0227.

Rubinstein, S. M., Cohen, G., Fineberg, J., Jun 2006. Contact area measurements reveal loading-history dependence of static friction. Phys. Rev. Lett. 96 (256103).

Scholz, C., Molnar, P., Johnson, T., 1972. Detailed studies of frictional sliding of granite and implications for the earthquake mechanism. J. Geophys. Res 77 (32), 6392–6406.

Shi, Z., Ben-Zion, Y., 2006. Dynamic rupture on a bimaterial interface governed by slip-weakening friction. Geophys. J. Int. 165 (2), 469–484.

Shi, Z., Ben-Zion, Y., Needleman, A., 2008. Properties of dynamic rupture and energy partition in a solid with a frictional interface. J. Mech. Phys. Solids 56 (1), 5–24.

Tang, C. A., Liu, H., Lee, P. K. K., Tsui, Y., Tham, L. G., 2000. Numerical studies of the influence of microstructure on rock failure in uniaxial compression — part i: effect of heterogeneity. International Journal of Rock Mechanics and Mining Sciences 37 (4), 555–569.

Wang, D., Mori, J., 2012. The 2010 qinghai, china, earthquake: A moderate earthquake with supershear rupture. Bull. Seismol. Soc. Am. 102 (1), 301–308.

Weertman, J., 1963. Dislocations moving uniformly on the interface between isotropic media of different elastic properties. J. Mech. Phys. Solids 11 (3), 197–204.

Weertman, J., 1980. Unstable slippage across a fault that separates elastic media of different elastic constants. J. Geophys. Res. 85(B3), 1455–1461.

Wriggers, P., 2006. Computational Contact Mechanics, 2nd Edition. Springer-Verlag, Berlin Heidelberg.

Xia, K., 1 2005. Laboratory investigations of earthquake dynamics. Ph.D. thesis, California Institute of Technology.

Xia, K., Rosakis, A. J., Kanamori, H., 2004. Laboratory earthquakes: the sub-rayleigh-to-supershear rupture transition. Science 303 (5665), 1859–61.

Xia, K., Rosakis, A. J., Kanamori, H., Rice, J. R., 2005. Laboratory earthquakes along inhomogeneous faults: Directionality and supershear. Science 308, 681–684.

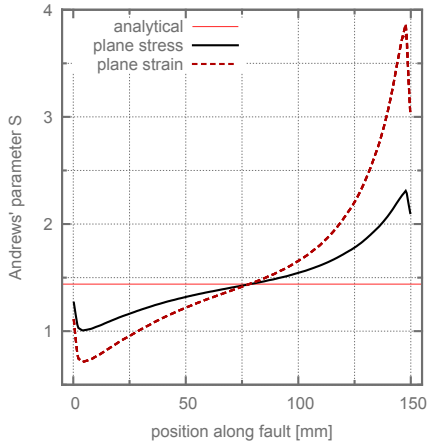

Figure A.1: Stress distribution along fault in plane stress and plane strain conditions for the fully unconfined configuration at $\beta = 20°$

Appendix A. Additional figures and tables

Appendix A.1. Stress distribution and rupture properties

Table A.1: Characteristics of dynamic rupture on a Homalite-100 / Polycarbonate interface for slip profiles of Figures 4

Property	Fully unconfined		Periodic	
	westward	eastward	westward	eastward
Pulse-like rupture, Figure 4a				
RMS slip [m]	$5.0 \cdot 10^{-5}$	$3.5 \cdot 10^{-5}$	$5.0 \cdot 10^{-5}$	$4.0 \cdot 10^{-5}$
v_{rupt} [m/s]	842	658	834	739
Potency [m^2]	$7.0 \cdot 10^{-6}$	$3.5 \cdot 10^{-6}$	$7.1 \cdot 10^{-6}$	$5.6 \cdot 10^{-6}$
Slip distance [mm]	144	108	144	144
RMS peak slip velocity [m/s]	2.5	1.5	2.4	1.8
Pulse-like rupture, Figure 4b				
RMS slip [m]	$6.0 \cdot 10^{-5}$	$4.8 \cdot 10^{-5}$	$6.0 \cdot 10^{-5}$	$5.3 \cdot 10^{-5}$
v_{rupt} [m/s]	846	770	848	792
Potency [m^2]	$8.5 \cdot 10^{-6}$	$6.7 \cdot 10^{-6}$	$8.4 \cdot 10^{-6}$	$7.5 \cdot 10^{-6}$
Slip distance [mm]	144	144	144	144
RMS peak slip velocity [m/s]	2.7	2.0	2.6	2.2
Crack-like rupture, Figure 4c				
RMS slip [m]	$11.3 \cdot 10^{-5}$	$11.1 \cdot 10^{-5}$	$11.3 \cdot 10^{-5}$	$11.5 \cdot 10^{-5}$
$v_{rupt}[m]$	866	811	857	818
Potency [m^2]	$15.6 \cdot 10^{-6}$	$15.3 \cdot 10^{-6}$	$15.5 \cdot 10^{-6}$	$15.8 \cdot 10^{-6}$
Slip distance [mm]	144	144	144	144
RMS peak slip velocity [m/s]	2.8	2.3	2.7	2.3

Appendix A.2. Dependence of rupture properties on roughness and static friction.

Comparing experimental data from the literature, Byerlee (1978) showed that rocks friction strongly depends on surface roughness, if normal stress is lower than 5 MPa. Xia (2005, page 78, Table 3.1) showed that surface roughness also plays a role in his experiments with much higher normal stresses. Based on Ohnaka (2003), Xia (2005) established roughness being related to D_c.

Xia (2005) used two different surface finishes, a rough and a smooth one. As the surface roughness at the material interface influences the slip-weakening distance (Ohnaka, 2003), we conducted simulations to explore the influence of D_c to our model configurations, the results are shown in Table A.2. We observe, that with increased roughness the supershear transition length increases which may lead to no supershear transition at all for a lower value of P.

In a similar fashion to Xia (2005, page 78, Table 3.1) our model shows roughness-dependent rupture behavior. Here we mainly compare our experimental setups in a qualitative way, so we abstain from using a pressure-dependent D_c, although it has been shown to be pressure dependent by Lu et al. (2009). The results for simulations with different D_c are shown in Table A.2.

Table A.3 shows parameter sweeps for static and dynamic coefficients of friction, where $\mu_s - \mu_d = 0.4$ as in section 3.

	$D_c = 4.1\,\mu$m								$D_c = 4.6\,\mu$m								$D_c = 5.5\,\mu$m								$D_c = 8.6\,\mu$m							
°\MPa	10	11	12	13	14	15	16	17	10	11	12	13	14	15	16	17	10	11	12	13	14	15	16	17	10	11	12	13	14	15	16	17
	periodic configuration																															
20.0							–	–																								
							–	–																								
20.5					–	–	–	–								–																
					–	–	–	–								–																
21.0				–	–	–	–	–						–	–	–							–	–								
				–	–	–	67	61						–	–	–							–	–								
21.5			–	–	–	–	–	–					–	–	–	–						–	–	–								
			–	64	55	49	44	40					–	67	59	52						–	73	59								
22.0		–	–	–	–	–	–	–			–	–	–	–	–	–				–	–	–	–	–								
		59	50	43	39	37	32	31			63	58	51	44	41	37				64	58	51	45	41								
22.5	–	–	–	–	–	–	–	–		–	–	–	–	–	–	–			–	–	–	–	–	–								–
	51	43	37	32	31	28	26	22		58	48	41	37	34	31	30			56	48	43	37	35	32								54
23.0	–	–	–	–	–	–	–	–	–	–	–	–	–	–	–	–		–	–	–	–	–	–	–					–	–	–	–
	37	32	30	27	24	21	17	7	51	43	36	32	30	28	26	22		49	41	36	33	30	28	26					51	45	41
23.5	–	–	–	–	–	–	–	–	–	–	–	–	–	–	–	–	–	–	–	–	–	–	–	–					–	–	–	–
	30	27	23	20	18	8	7	7	39	34	30	26	24	21	19	16	44	37	32	28	26	25	22	20					44	40	35	32
24.0	–	–	–	–	–	–	–	8	–	–	–	–	–	–	–	–	–	–	–	–	–	–	–	–				–	–	–	–	–
	24	21	18	8	7	7	6	6	31	26	24	21	19	16	7	7	35	30	26	24	21	19	17	8				40	35	31	28	26
24.5	–	–	–	–	–	–	7	7	–	–	–	–	–	–	–	–	–	–	–	–	–	–	–	–			–	–	–	–	–	–
	19	16	8	7	6	6	6	6	25	22	19	16	9	7	7	6	27	24	21	19	16	10	7	7			36	32	28	26	23	22
25.0	–	–	67	48	7	7	6	6	–	–	–	–	–	55	17	7	–	–	–	–	–	–	71	42		–	–	–	–	–	–	–
	14	8	7	6	6	6	6	5	20	17	13	8	7	6	6	6	22	20	17	14	8	7	6	6		35	29	26	23	21	19	17
	confined configuration																															
20.0								–																								
20.5							–	–																								
							–	–																								
21.0					–	–	–	–							–	–																
					–	–	–	–							–	–																
21.5				–	–	–	–	–						–	–	–							–	–								
				–	–	–	–	–						–	–	–							–	–								
22.0			–	–	–	–	–	–					–	–	–	–						–	–	–								
			–	–	–	–	–	50					–	–	–	–						–	–	–								
22.5		–	–	–	–	–	–	–			–	–	–	–	–	–				–	–	–	–	–								
		–	–	56	47	41	37	36				–	–	–	51	42					–	–	–	53								
23.0	–	–	–	–	–	–	–	–		–	–	–	–	–	–	–			–	–	–	–	–	–								–
	56	50	41	37	34	33	31	30			59	49	41	39	35	33			72	59	49	45	39	36								57
23.5	–	–	–	70	70	68	67	74	–	–	–	–	–	70	68	68		–	–	–	–	–	70	68							–	–
	44	37	33	30	28	28	24	22		48	41	37	33	32	30	28		48	47	41	37	33	32	30							48	45
24.0	64	61	56	54	53	50	48	45	72	63	64	61	56	56	53	52	–	72	72	64	61	56	56	53					–	57	68	73
	34	31	28	26	23	21	8	7	43	36	32	31	28	27	24	23	43	40	35	32	31	28	27	24					42	43	39	35
24.5	51	48	46	45	42	39	38	33	51	52	49	49	48	46	43	41	49	51	51	49	49	48	46	45				51	48	48	49	51
	28	26	23	20	16	7	7	7	34	30	28	26	23	21	19	9	36	33	29	28	26	23	21	20				40	38	36	32	30
25.0	42	41	38	34	33	24	9	7	44	44	42	41	39	36	34	31	44	44	44	42	41	39	38	34			43	40	41	41	41	42
	24	21	17	8	7	7	6	6	29	26	23	21	18	15	7	7	31	28	26	23	21	18	16	8			39	34	31	30	26	26

Table A.2: Supershear transition lengths in millimeters from the center of the nucleation patch for different slip-weakening distances. Each cell contains the supershear transition length in the westward (positive) direction as the upper value and in the eastward (negative) direction as the lower value. Rupture did not reach the fault end for empty entries, it reached the end without a supershear transition for '–'.

	Confined								Horizontally unconfined								Fully unconfined								Periodic							
°\MPa	10	11	12	13	14	15	16	17	10	11	12	13	14	15	16	17	10	11	12	13	14	15	16	17	10	11	12	13	14	15	16	17
	$\mu_s = 0.57,\ \mu_d = 0.17$																															
20.0						–	–	–				–	–	–	–	–				–	–	–	–	–				–	–	–	–	–
						–	–	–				–	–	–	–	–				–	–	–	–	–				64	64	56	49	44
20.5				–	–	–	–	–			–	–	–	–	–	–			–	–	–	–	–	–			–	–	–	–	–	–
				–	–	–	–	–			–	–	–	–	–	–			–	–	–	–	–	–			59	51	44	40	37	32
21.0			–	–	–	–	–	–		–	–	–	–	–	–	–		–	–	–	–	–	–	–		–	–	–	–	–	–
			–	–	52	52	42	39		–	–	–	–	–	44	42		–	–	–	–	41	36	32		50	43	37	34	30	28	27
21.5		–	–	–	–	–	–	–	–	–	–	–	–	–	–	–	–	–	–	–	–	–	–	–	–	–	–	–	–	–	–	–
		54	52	44	38	36	32	31	–	–	–	48	38	33	30	26	–	–	46	36	32	28	27	23	44	37	34	29	27	25	22	21
22.0	–	–	–	68	68	66	63	58	–	–	–	–	–	–	–	–	–	–	–	–	–	–	–	–	–	–	–	–	–	–	–	–
	47	43	37	34	31	28	28	25	–	43	36	31	28	24	20	17	68	36	31	27	24	22	19	16	34	30	26	24	22	19	18	12
22.5	54	56	54	53	51	50	49	47	–	–	70	70	66	71	51	46	–	–	–	–	–	–	–	–	–	–	–	–	–	–	–	–
	37	32	31	28	25	24	22	19	36	29	26	22	19	16	8	7	32	27	23	20	19	16	8	7	27	24	22	19	17	14	8	7
23.0	47	47	45	45	43	41	40	36	62	55	51	45	40	32	17	8	–	–	–	65	57	50	43	15	–	–	–	–	–	–	–	–
	31	27	26	23	21	19	16	8	27	23	19	16	11	7	7	7	24	22	19	16	9	7	7	6	22	20	17	14	9	7	7	6
23.5	40	40	38	36	35	29	24	17	42	38	32	22	16	8	7	6	56	51	45	38	23	10	8	7	–	–	–	–	59	22	8	7
	26	23	21	19	17	9	7	7	21	17	15	8	7	6	6	6	19	16	13	8	7	6	6	6	19	15	12	8	7	6	6	6
24.0	32	30	28	26	23	17	9	7	27	22	15	9	7	7	6	6	38	31	19	12	8	7	6	6	62	49	36	17	9	7	6	6
	22	19	17	14	8	7	6	6	16	11	8	7	6	6	6	6	16	11	7	6	6	6	6	6	14	9	7	6	6	6	6	5
24.5	27	23	18	16	10	7	7	6	16	11	8	7	6	6	6	6	19	14	9	7	6	6	6	6	26	16	11	8	7	6	6	6
	18	16	10	7	7	6	6	6	11	7	7	6	6	6	5	5	10	7	6	6	6	6	5	5	9	7	6	6	6	5	5	5
25.0	18	16	11	8	7	6	6	6	10	8	7	6	6	5	5	5	11	8	7	6	6	6	6	5	13	9	7	6	6	6	6	5
	15	9	7	7	6	6	6	5	8	6	6	5	5	5	5	5	7	6	6	6	5	5	5	5	7	6	6	6	5	5	5	5
	$\mu_s = 0.63,\ \mu_d = 0.23$																															
20.0																																
20.5																–																
21.0																–																
21.5															–	–							–	–							–	–
															–	–							–	–							–	–
22.0							–	–					–	–	–	–					–	–	–	–					–	–	–	–
								–					–	–	–	–					–	–	–	–					–	–	–	–
22.5						–	–	–				–	–	–	–	–				–	–	–	–	–				–	–	–	–	–
						–	–	–				–	–	–	–	–				–	–	–	–	–				–	–	–	–	–
23.0				–	–	–	–	–		–	–	–	–	–	–	–			–	–	–	–	–	–			–	–	–	–	–	–
					–	–	–	–			–	–	–	–	–	–			–	–	–	–	–	–			–	–	64	54	51	44
23.5			–	–	–	–	–	–	–	–	–	–	–	–	–	–		–	–	–	–	–	–	–		–	–	–	–	–	–	–
			–	–	–	–	–	–		–	–	–	–	–	–	–		–	–	–	–	–	–	–	46	73	56	49	44	39	37	34
24.0		–	–	–	–	–	–	–	–	–	–	–	–	–	–	–	–	–	–	–	–	–	–	–	–	–	–	–	–	–	–	–
		–	–	54	53	43	40	37	–	–	–	–	–	49	42	37	–	–	–	–	44	39	34	31	56	48	41	37	34	31	28	27
24.5	–	–	–	–	–	–	–	–	–	–	–	–	–	–	–	–	–	–	–	–	–	–	–	–	–	–	–	–	–	–	–	–
	64	53	46	40	36	34	33	31	–	–	58	39	34	30	27	7	–	54	39	34	31	27	23	8	41	37	31	29	27	23	21	7
25.0	–	–	–	–	71	71	70	68	–	–	–	–	–	–	–	71	–	–	–	–	–	–	–	–	–	–	–	–	–	–	–	–
	47	39	35	32	31	30	27	26	51	37	32	28	23	8	7	7	39	32	28	24	21	8	7	7	32	28	26	22	20	8	7	6

Table A.3: Here we show the sensitivity of supershear transition length to a change in static and dynamic friction. The numerical nucleation method and $D_c = 5\,\mu$m are used.

Appendix A.3. Experimental nucleation method

In laboratory experiments with an exploding wire mechanism (Xia et al., 2004) it is likely to obtain similar stress for each triggering and a nucleation mechanism independent of the applied pressure P. Thus in a second nucleation method (called the *experimental nucleation method*) we assure a uniform stress drop for all simulations. Detailed work on this kind of rupture nucleation has been done by Lu et al. (2009). They determined the stress drop for rupture nucleation as $(|\sigma_N| - \Delta\sigma)(\mu_s - \mu_d) < |\tau|$ where they chose the smallest $\Delta\sigma$ over all their simulations. Here σ_N is the normal fault strength and $\Delta\sigma$ is the normal stress drop for a certain simulation. Our nucleation mechanism works in a similar fashion. However, we distinguish between dynamic and static stress drop, where for rupture initiation only the static stress drop is applied to the nucleation patch. Then, according to the friction law in equation 4 the stress drops further by a dynamic stress drop, which is also uniform for all simulations. The result is very similar to the slow increase of $\Delta\sigma$ at nucleation initiation in Lu et al. (2009), as well as its decrease.

To determine the stress drop most appropriate for nucleation, we first determine the highest static coefficient to which we could lower the friction in the nucleation patch and initiate rupture in all simulations (with various stresses and fault inclinations). For a higher pressure P, the Coulomb failure stress is further away from failure than for lower P. Thus the stress drop necessary for nucleation of the highest P defines our static stress drop. In a next step the dynamic stress drop for the nucleation site has to be defined. To make our simulations comparable, we should either prevent the interface from opening in the nucleation patch or choose a value to open the interface in all simulation. On this matter we follow Lu et al. (2009) and choose the largest dynamic stress drop in a way that prevents opening of the fault. This is obtained by solving $\Delta\sigma_d = -(|\tau| / |\sigma_N| + \Delta\sigma_s/\sigma_N)$ for all considered simulations, where $\Delta\sigma_s$ is the minimum static stress drop over all simulations and $\Delta\sigma_d$ is the dynamic stress drop in the nucleation point. Finally, the smallest value of $\Delta\sigma_d$ is chosen to be the dynamic stress drop. This method allows for a well-defined nucleation with equal stress drops for all simulations. However increasing pressure P increases the stress drop necessary to initiate rupture and changes the 'overshoot' of the Coulomb failure stress. It is therefore necessary to conduct detailed studies to separate the effect of this overshoot on the rupture propagation from the influences of various angles β and pressures P. Supershear transition lengths for this method are shown in Table A.4.

	Confined								Fully unconfined								Periodic							
°\MPa	10	11	12	13	14	15	16	17	10	11	12	13	14	15	16	17	10	11	12	13	14	15	16	17
	Smooth surface - $D_c = 3.7\,\mu$m ($V_c = 0.17\,$m/s, $\tau_c = 22\,\mu$s)																							
20.0		-	-	-	-	-	-	-		-	-	-	-	-	-	-		-	-	-	-	-	-	-
				-	-					-	-	-	-	-				-	-	-	-	-		
20.5	-	-	-	-	-	-	-	-	-	-	-	-	-	-	-	-	-	-	-	-	-	-	-	-
		-	-	-	-				-	-	-	-	-	-	-		-	-	-	-	-	-	-	
21.0	-	-	-	-	-	-	-	-	-	-	-	-	-	-	-	-	-	-	-	-	-	-	-	-
	-	-	-	-	-	-			-	-	-	-	-	-	-	-	-	-	-	-	66	55	49	44
21.5	-	-	-	-	-	-	-	-	-	-	-	-	-	-	-	-	-	-	-	-	-	-	-	-
	-	-	-	-	-	-	-		-	-	8	10	10	10	10	10	-	68	54	49	45	41	37	32
22.0	-	-	-	-	-	-	-	-	-	-	-	-	-	-	-	-	-	-	-	-	-	-	-	-
	-	-	-	-	47	43	42	38	10	11	14	7	7	7	7	7	52	47	43	38	7	7	7	7
22.5	-	-	-	-	-	-	-	-	-	-	-	-	-	-	-	-	-	-	-	-	-	-	-	-
	-	-	45	42	39	36	32	31	15	7	6	6	7	6	6	6	41	26	7	7	6	6	6	6
23.0	-	-	-	-	-	71	71	69	-	-	8	9	9	9	11	10	-	-	8	8	8	8	8	9
	43	41	37	23	7	7	7	7	7	6	6	6	6	6	6	6	7	6	6	6	6	6	6	6
23.5	72	68	74	56	56	52	52	50	8	7	7	7	7	7	6	6	8	8	7	13	7	7	7	7
	37	6	7	7	7	7	6	6	6	6	6	6	6	6	6	6	6	6	6	6	6	6	6	6
24.0	54	53	48	42	7	7	7	7	7	7	7	6	6	6	6	6	8	7	7	6	6	6	6	6
	7	6	6	6	6	6	6	6	5	5	5	5	5	5	5	5	5	5	5	5	5	5	5	5
24.5	42	7	7	7	7	6	6	6	6	6	6	6	6	6	6	6	7	6	6	6	6	6	6	6
	6	6	6	6	6	6	6	6	5	5	5	5	5	5	5	5	5	5	5	5	5	5	5	5
25.0	7	6	6	6	6	6	6	6	5	5	5	5	5	5	5	5	6	5	6	5	5	5	5	5
	5	5	5	5	5	5	5	5	5	5	5	5	5	5	5	5	5	5	5	5	5	5	5	5
	Rough surface - $D_c = 7.0\,\mu$m ($V_c = 0.24\,$m/s, $\tau_c = 29\,\mu$s)																							
20.0					-	-	-	-							-	-							-	-
20.5						-	-	-								-								-
21.0							-	-							-	-								-
															-	-								-
21.5								-			-	-	-	-	-	-			-	-	-	-	-	-
												-	-	-	-	-				-	-	-	-	-
22.0			-	-	-	-	-	-		-	-	-	-	-	-	-		-	-	-	-	-	-	-
					-	-	-			-	-	-	-	-	-	-		-	-	-	-	65	58	52
22.5		-	-	-	-	-	-	-	-	-	-	-	-	-	-	-	-	-	-	-	-	-	-	-
			-	-	-	-	-	-	-	-	-	-	-	-	-	-	-	-	71	60	53	47	43	38
23.0	-	-	-	-	-	-	-	-	-	-	-	-	-	-	-	-	-	-	-	-	-	-	-	-
	-	-	-	-	-	56	52	45	-	-	-	-	-	45	68	40	71	59	51	45	40	37	34	31
23.5	-	-	-	-	-	-	-	-	-	-	-	-	-	-	-	-	-	-	-	-	-	-	-	-
	-	-	56	57	47	41	37	35	10	11	9	47	41	36	32	28	53	43	41	37	34	30	28	25
24.0	-	-	-	69	67	67	59	57	-	-	-	-	-	-	-	-	-	-	-	-	-	-	-	-
	63	54	49	39	36	33	32	30	7	55	41	35	28	22	7	7	41	37	34	29	22	20	7	7
24.5	68	67	58	55	65	51	49	48	-	8	7	-	-	-	-	63	-	8	8	-	-	-	-	-
	49	39	36	34	30	28	26	24	41	33	6	6	6	6	6	7	34	7	7	6	6	6	7	7
25.0	73	68	49	46	42	41	39	38	7	7	64	56	49	44	32	7	8	8	8	7	7	7	11	61
	39	34	32	28	24	21	18	7	6	6	6	6	6	6	6	6	6	6	6	6	6	6	6	6

Table A.4: The ruptures for these parameter sweeps have been nucleated by the experimental nucleation method. The upper half of the table shows transition lengths in millimeters for a smooth surface, the lower half shows transition lengths for a rough surface.

	Confined								Fully unconfined								Periodic							
°\MPa	10	11	12	13	14	15	16	17	10	11	12	13	14	15	16	17	10	11	12	13	14	15	16	17
	$\mu_s = 0.57,\ \mu_d = 0.17$																							
20.0		–	–	–	–	–			–	–	–	–	–	–	–	–	–	–	–	–	71	60	53	44
		–	–	–	–	–			–	–	–	–	–	–	–	–	–	–	–	–				
20.5	–	–	–	–	–	–	–	–	–	–	–	–	–	–	–	–	–	–	–	–	–	–	–	–
		–	–	–	–	–	–		–	–	–	–	–	–	–	–	–	71	60	52	44	41	39	35
21.0	–	–	–	–	–	–	–	–	–	–	–	–	–	–	–	–	–	–	–	–	–	–	–	–
	–	–	–	–	–	45	42	40	–	–	7	10	10	10	45	34	58	49	44	40	37	34	31	27
21.5	–	–	–	–	–	–	–	–	–	–	–	–	–	–	–	–	–	–	–	–	–	–	–	–
	–	–	40	44	41	38	36	31	8	11	41	50	37	7	7	7	43	41	37	32	22	7	7	7
22.0	–	–	–	71	70	68	68	72	–	–	–	–	–	–	–	–	–	–	–	–	–	–	–	–
	58	43	38	38	34	31	28	25	47	41	26	6	6	6	6	6	37	32	7	6	6	6	7	6
22.5	69	66	73	56	53	49	47	44	–	–	8	7	10	7	7	7	–	–	8	8	9	7	11	13
	37	37	32	31	7	7	7	7	31	6	6	6	6	6	6	6	7	6	6	6	6	6	6	6
23.0	65	49	45	45	41	38	34	30	8	7	63	7	7	7	6	6	8	8	7	7	7	7	6	6
	34	30	7	7	7	7	7	7	6	6	6	6	6	6	6	6	6	6	6	6	6	6	6	6
23.5	43	40	36	12	7	7	7	7	51	7	6	6	6	6	6	6	7	7	7	6	6	6	6	6
	7	6	6	6	6	6	6	6	5	5	5	5	5	5	5	5	5	5	5	5	5	5	6	5
24.0	33	7	7	7	7	7	6	6	6	6	6	6	6	6	6	6	6	6	6	6	6	6	6	5
	6	6	6	6	6	6	6	6	5	5	5	5	5	5	5	5	5	5	5	5	5	5	5	5
24.5	7	6	6	6	6	6	6	6	5	5	5	5	5	5	5	5	6	5	5	5	5	5	5	5
	6	5	5	5	5	5	5	5	5	5	5	5	5	5	5	5	5	5	5	5	5	5	5	5
25.0	6	6	6	5	5	5	5	5	5	5	5	5	5	5	5	5	5	5	5	5	5	5	5	5
	5	5	5	5	5	5	5	5	5	5	5	5	5	5	5	5	5	5	5	5	5	5	5	5
	$\mu_s = 0.63,\ \mu_d = 0.23$																							
20.0				–	–	–	–	–					–	–	–	–					–	–	–	–
20.5					–	–	–	–						–	–	–						–	–	–
21.0					–	–	–	–							–	–							–	–
21.5						–	–	–				–	–	–	–	–					–	–	–	–
														–	–							–		
22.0						–	–	–		–	–	–	–	–	–	–			–	–	–	–	–	–
											–	–	–	–	–				–	–	–	–	–	
22.5		–	–	–	–	–	–	–	–	–	–	–	–	–	–	–	–	–	–	–	–	–	–	–
			–	–	–	–				–	–	–	–	–	–	–		–	–	–	–	–	–	–
23.0	–	–	–	–	–	–	–	–	–	–	–	–	–	–	–	–	–	–	–	–	–	–	–	–
		–	–	–	–	–	–		–	–	–	–	–	–	–	–	–	–	–	–	66	58	51	44
23.5	–	–	–	–	–	–	–	–	–	–	–	–	–	–	–	–	–	–	–	–	–	–	–	–
	–	–	–	–	–	–	–	43	–	8	–	–	–	–	–	43	–	71	58	49	44	41	37	34
24.0	–	–	–	–	–	–	–	–	–	–	–	–	–	–	–	–	–	–	–	–	–	–	–	–
	–	–	–	–	66	45	40	37	11	12	13	12	45	41	36	31	55	49	44	40	36	32	28	26
24.5	–	–	–	–	–	–	–	–	–	–	–	–	–	–	–	–	–	–	–	–	–	–	–	–
	–	58	46	40	36	36	33	31	16	6	41	7	7	7	7	7	43	39	7	7	7	7	7	7
25.0	–	–	–	71	71	71	70	68	–	–	–	–	–	–	–	–	–	8	–	–	–	–	–	–
	50	40	37	34	31	30	27	26	35	6	6	6	6	6	6	6	6	6	6	6	6	6	6	6

Table A.5: Here we show the sensitivity of supershear transition length to a change in static and dynamic friction. The experimental nucleation method and $D_c = 5\,\mu$m are used.